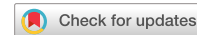


# communications

## earth & environment

### ARTICLE



<https://doi.org/10.1038/s43247-021-00182-y> OPEN

## Horizontal circulation across density surfaces contributes substantially to the long-term mean northern Atlantic Meridional Overturning Circulation

Rong Zhang  <sup>1✉</sup> & Matthew Thomas<sup>1,2</sup>

The Greenland Sea is often viewed as the northern terminus of the Atlantic Meridional Overturning Circulation. It has also been proposed that the shutdown of open-ocean deep convection in the Labrador or Greenland Seas would substantially weaken the Atlantic Meridional Overturning Circulation. Here we analyze Robust Diagnostic Calculations conducted in a high-resolution global coupled climate model constrained by observed hydrographic climatology to provide a holistic picture of the long-term mean Atlantic Overturning Circulation at northern high latitudes. Our results suggest that the Arctic Ocean, not the Greenland Sea, is the northern terminus of the mean Atlantic Overturning Circulation; open-ocean deep convection, in either the Labrador or Greenland Seas, contributes minimally to the mean Atlantic Overturning Circulation, hence it would not necessarily be substantially weakened by a shutdown of open-ocean deep convection; horizontal circulation across sloping isopycnals contributes substantially (more than 40%) to the maximum mean northeastern subpolar Atlantic Overturning Circulation.

<sup>1</sup> National Oceanic and Atmospheric Administration, Geophysical Fluid Dynamics Laboratory, Princeton, NJ, USA. <sup>2</sup> University Corporation for Atmospheric Research, Boulder, CO, USA. ✉email: [Rong.Zhang@noaa.gov](mailto:Rong.Zhang@noaa.gov)

The Atlantic Meridional Overturning Circulation (AMOC) has profound impacts on climate<sup>1–4</sup>. How and why the AMOC changes in the modern climate remains a challenging issue<sup>5,6</sup>. Unlike many other climate variables, there is no established long-term mean state of directly observed AMOC over the past several decades to serve as a reference for historical and future AMOC changes. Hence it is difficult to know whether the current/future observed AMOC is different from its long-term mean state in the historical context.

Climate models are often used to simulate historical and future AMOC changes, and commonly project a substantial future AMOC weakening due to the shutdown of open-ocean deep convection in the Labrador Sea and Greenland Sea<sup>7,8</sup>. A dominant contribution of Labrador Sea deep convection to the AMOC is simulated in many climate models<sup>7,8</sup>, but this has been challenged by observational analyses<sup>9–17</sup>. For example, the net AMOC contribution from the Labrador Sea is found to be mainly from boundary sinking, and is estimated to be only ~1Sv (~2Sv) in depth (density) coordinates from hydrographic observations taken during a period of strong Labrador Sea deep convection (1990–1997)<sup>11</sup>. Similar estimates are found over the recent decade (2002–2016)<sup>13</sup>. Observations further indicate that a strengthening of the Labrador Sea western boundary outflow (including the intermediate level) occurred from the late 1990s to early 2000s despite a concurrent weakening of Labrador Sea deep convection<sup>10</sup>. Recent observations from the Overturning in the Subpolar North Atlantic Program (OSNAP), taken during a period of strong Labrador Sea deep convection (2014–2016), showed that the AMOC across the OSNAP section (see locations in Fig. 1) is dominated by the eastern component and not by that across the Labrador Sea<sup>16,17</sup>. Since direct OSNAP observations cover only a short period, and only the subpolar North Atlantic<sup>16,17</sup>, it is unclear whether this short-term result represents a long-term feature and holds over the past several decades, nor whether the contribution of Greenland Sea deep convection to the AMOC is similarly small as that of Labrador Sea deep convection.

It is often viewed that in the modern climate the Nordic Seas (e.g. the Greenland Sea) are the northern terminus of the AMOC and the dense water formation processes within the Nordic Seas provide the densest source water for downstream overflows across the Greenland-Scotland Ridge (GSR)<sup>18–20</sup>. Greenland Sea deep convection is often investigated in both observational studies<sup>19,20</sup> and climate models<sup>7,8</sup> as an important source for AMOC-associated GSR overflows (see locations in Fig. 1), but its importance has similarly been questioned by analyses of observed hydrographic data<sup>21–24</sup>. However, without an observational-based estimate of the long-term mean AMOC to calibrate the mean state AMOC structure in climate models, such as the source of the densest water for the mean AMOC and the contributions of the deep convection in the Labrador and Greenland Seas to the mean AMOC, it is still challenging to determine whether model-simulated historical and future AMOC changes are reliable.

In this study, robust diagnostic calculations (RDC) are conducted using a high-resolution global coupled climate model in conjunction with the observed hydrographic climatology to provide a holistic picture of the long-term mean AMOC structure at northern high latitudes (a key region for AMOC changes, see the schematic Fig. 1) over the past several decades. The RDC method was originally proposed by Sarmiento and Bryan<sup>25</sup>, in which the potential temperature and salinity in ocean models are restored back to the observed hydrographic fields to produce dynamically consistent velocity fields. The RDC approach has been applied to regional ocean-only models<sup>25,26</sup>, a global ocean-ice coupled model<sup>27</sup>, and a global ocean model coupled to a two-dimensional atmospheric energy balance model and a slab sea ice

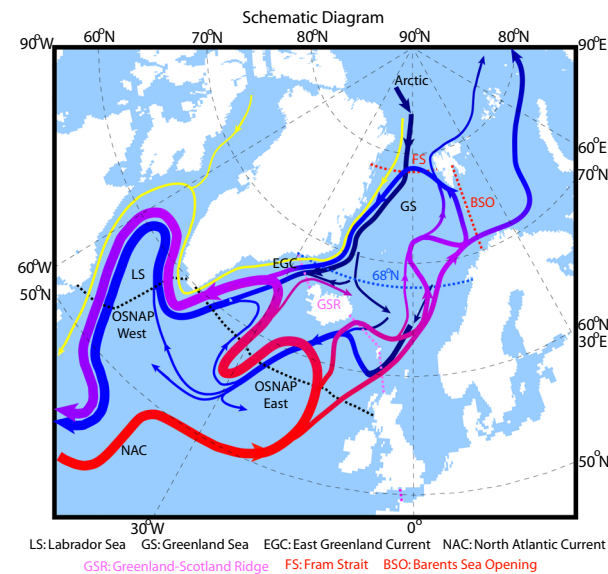


**Fig. 1 Schematic of long-term mean AMOC pathways.** The schematic circulation is revised from ref. <sup>66</sup> based on robust diagnostic calculation (RDC) results and overlapped with sections (dotted lines). Colors of arrows indicate seawater density (light to dense: yellow-red-purple-violet-blue-dark blue). The density of Atlantic inflow increases along the pathways of the northeastern subpolar gyre, the gyre extended into Nordic Seas, and the branches entering the Arctic through BSO and east FS. Dark blue arrows: dense outflow through the Nordic Seas. The overflows become lighter after passing through the GSR due to entrainments. Yellow arrows: light (cold fresh) surface currents. In addition to the non-Ekman depth-space AMOC component linked to the density contrast across a section, the northeastern subpolar gyre and the gyre extended into the Nordic Seas moving with changing densities also contribute to the density-space AMOC. The density contrast across OSNAP East is much larger than that across OSNAP West, consistent with a much stronger AMOC across OSNAP East.

model<sup>28</sup>. Here the RDC experiments are conducted using a high-resolution global fully coupled climate model, in which the ocean potential temperature and salinity are relaxed back to the observed long-term mean hydrographic data (see “Methods”) to produce the long-term mean velocity fields, especially over the extratropical North Atlantic and the Arctic Mediterranean. For comparison, the high-resolution global coupled climate model<sup>29</sup> used for the RDC experiments is also employed to generate a present-day control simulation (see “Methods”).

This RDC-estimated long-term mean AMOC structure (across both monitored and un-monitored sections) over the extratropical North Atlantic and the Arctic Mediterranean could be used to interpret future observed AMOC changes and guide modeling/observational efforts. Our results suggest that open-ocean deep convection in either the Labrador or Greenland Seas contributes minimally to the long-term mean AMOC strength. Hence a shutdown of open-ocean deep convection in the Labrador and Greenland Seas would not necessarily weaken the AMOC substantially. However, reducing the upper-ocean density along the East Greenland Current (EGC) could weaken the AMOC. We find that in the mean state, the deep AMOC branch across the Fram Strait (FS)/Barents Sea Opening (BSO) section (i.e., Arctic outflow) provides the densest source water for downstream overflows, and the Arctic Ocean, not the Greenland Sea, is the northern terminus of the mean AMOC. Our analyses also show that the horizontal circulation across sloping isopycnals contributes substantially to the long-term mean northeastern subpolar AMOC and provides an additional important physical

mechanism for why the long-term mean AMOC is much larger across the northeastern subpolar North Atlantic than that across the Labrador Sea. The recent directly observed northeastern subpolar AMOC across the OSNAP East subsection during 2014–2016<sup>16,17</sup> (a period of strong Labrador Sea deep convection) is weaker than the RDC-estimated long-term mean strength. It is important for climate models to faithfully simulate the mean AMOC structure to avoid overpredictions of the role of open-ocean deep convection in future AMOC changes, and for accurate predictions/projections of future AMOC changes induced by other important physical processes such as changes in the upper-ocean density along the EGC.

## Results

**The climatological mean sea surface height (SSH).** The long-term mean SSH in the RDC experiment compares very well with the satellite-observed mean dynamic topography (see “Methods”) (Fig. 2a, b, Supplementary Fig. 1a, b). They both reveal a realistic Gulf Stream separation and a realistic North Atlantic Current (NAC) pathway moving into the northwest corner

and contributing to the cyclonic subpolar gyre, as well as the gyre extension into the Nordic Seas (Fig. 2a, b). Conversely, the control simulation exhibits typical deficiencies in the Gulf Stream separation and the NAC pathway (shifting too far east and missing the northwest corner) (Fig. 2c), as found in many climate models mainly due to deficiencies in simulated Nordic Seas overflow<sup>28,30,31</sup>. The cyclonic gyre in the control simulation is too strong and the associated mean SSH is about 0.3m lower than that in the RDC experiment in the Labrador Sea (Fig. 2c) due to overestimated deep convection there (Supplementary Fig. 2).

**The AMOC across the OSNAP section.** Our RDC experiment shows that the long-term mean AMOC strength across the OSNAP section is also dominated by the OSNAP East component, and not by that across OSNAP West, in both density- and depth-space (Fig. 3). This result complements recent 21-month mean OSNAP observations<sup>16,17</sup> (Fig. 3) and is representative of the long-term climatology, suggesting that the observations are not just a short-term feature over the OSNAP period. In both the RDC experiment and the OSNAP observations, the maximum mean AMOC occurs at a denser level across OSNAP West than that across OSNAP East (Fig. 3a, b), and the maximum mean density-space AMOC across the entire OSNAP section is not larger than that across OSNAP East but is instead shifted to a slightly denser level (Fig. 3b, c). While similar results are found in the control simulation, the AMOC is shallower and shifts to lower densities (Fig. 3) due to model biases<sup>31</sup>. Similar control simulation results (i.e., the mean AMOC across the OSNAP section is dominated by the eastern rather than the western component) and biases (i.e., shallower and less dense mean AMOC) are also found in another coupled climate model as reported in a recent study<sup>32</sup>. Additional RDC experiments (see “Methods”) show that if an observed hydrographic climatology that does not resolve the low salinity/density along the EGC is used instead (Supplementary Fig. 3), then the estimated AMOC across OSNAP East and the entire section is stronger, especially in density-space (Supplementary Fig. 4).

Across the OSNAP section, the long-term mean velocity, density, and temperature/salinity from the RDC experiment compare well in general with recent observations (Fig. 4a, b, Supplementary Fig. 5a-d). The warm salty upper North Atlantic water becomes cold fresh along the pathways of the Atlantic inflow at the northern high latitudes. Across OSNAP East, the long-term mean upper ocean density contrast is dominated by the temperature contrast, with relatively warmer temperatures in the eastern subpolar gyre, and not by the salinity contrast (Fig. 4b, Supplementary Fig. 5c, d). Across OSNAP West, the long-term mean temperature contrast is smaller than that across OSNAP East (Supplementary Fig. 5c), and the salinity contrast has a stronger relative contribution to the density contrast that compensates for the temperature contrast due to the relatively colder temperatures and thus smaller thermal expansion coefficient there, resulting in a much smaller long-term mean density contrast than that across OSNAP East (Fig. 4b, Supplementary Fig. 5c, d). This is despite the presence of deep convection in the interior Labrador Sea (Supplementary Fig. 2a). It also explains the much smaller long-term mean depth-space AMOC across OSNAP West than that across OSNAP East (Fig. 3d, e), since the non-Ekman depth-space AMOC component (i.e., thermal wind contribution) is closely linked to the density contrast across a section<sup>33–35</sup>. The small long-term mean density contrast in the RDC experiment between the Labrador Sea boundary inflow and outflow is consistent with OSNAP observations<sup>17</sup> (Fig. 4a), as well as with hydrographic observations taken during periods with both weak and strong Labrador Sea deep convection<sup>36</sup>.

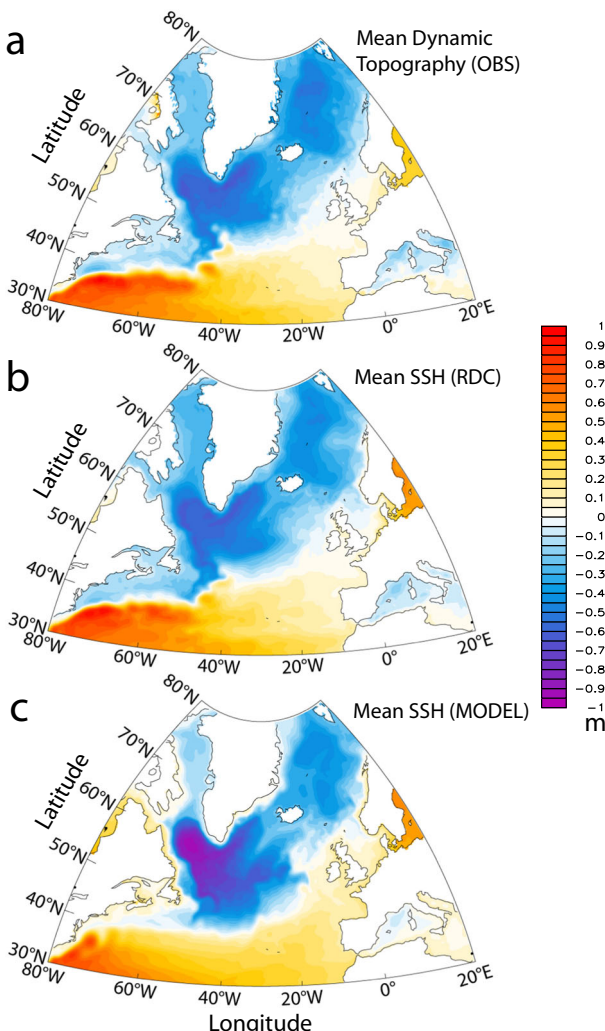


**Fig. 2 Mean dynamic topography/sea surface height (SSH, m) at northern high latitudes.** **a** Satellite observed (OBS) mean dynamic topography. **b** Mean SSH from robust diagnostic calculation (RDC). **c** Mean SSH from control simulation (MODEL). All are referenced to their own averages over the domain (80°W–20°E, 30°–80°N) and serve as streamlines of mean surface geostrophic circulation.

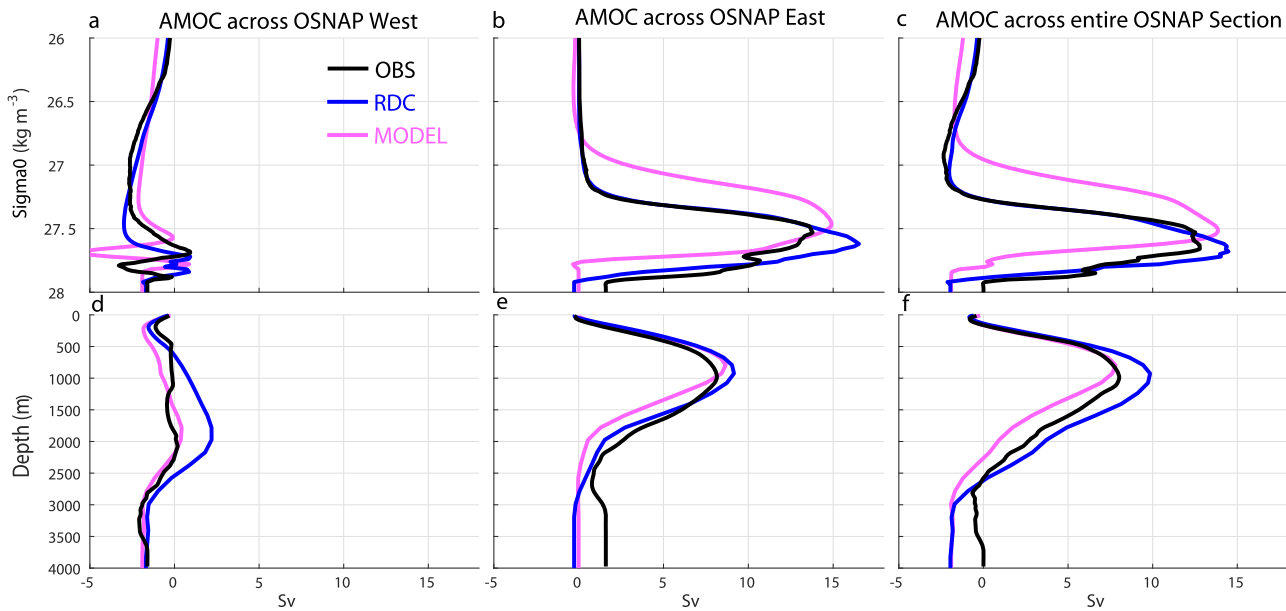


**Fig. 3 Mean AMOC streamfunctions (Sv,  $1\text{Sv} = 10^6 \text{m}^3 \text{s}^{-1}$ ) across the OSNAP section. a-c** Density-space (potential density  $\sigma_0$ ,  $\text{kg m}^{-3}$ ). **d-f** Depth-space (m). **a, d** OSNAP West. **b, e** OSNAP East. **c, f** Entire OSNAP section. Black: 21-month mean from OSNAP observations (OBS); Blue: robust diagnostic calculation (RDC); Pink: Control simulation (MODEL).

The control simulation has unrealistically stronger Labrador Sea deep convection than that in the RDC experiment (Supplementary Fig. 2). Yet, it still simulates a small density contrast between the Labrador Sea boundary inflow and outflow despite the dome-shaped isopycnals and high interior density induced by strong deep convection (Fig. 4c), resulting in a similarly small depth-space AMOC across OSNAP West (Fig. 3d). This demonstrates that the AMOC across OSNAP West is insensitive to Labrador Sea deep convection if the density contrast between the boundary inflow and outflow remains small.

In the RDC experiment, the Iceland-Scotland overflow moves along several interior pathways after passing southward across OSNAP East at the eastern side of the Reykjanes Ridge (see Figs. 1 and 5 for locations), not just along the single pathway turning northward at the western side of the Reykjanes Ridge into the Irminger Sea, suggesting that the recent observed interior Iceland-Scotland overflow pathways near the Charlie-Gibbs Fracture Zone<sup>37</sup> are a long-term feature.

**The horizontal circulation contribution to the AMOC across the OSNAP section.** In addition to the depth-space AMOC, the cyclonic northeastern subpolar horizontal circulation that flows across sloping isopycnals also contributes substantially to the density-space AMOC across OSNAP East (Fig. 5). The lighter (denser) branch of the cyclonic northeastern subpolar gyre moves northward in the interior and eastern side of the basin (southward near the western boundary) above (below) the sloping isopycnal at which the maximum AMOC occurs (Figs. 4, 5). The strong slope of this isopycnal results in a much larger maximum AMOC in density-space than that in depth-space across OSNAP East (Fig. 3b, e). The positive inflow and negative outflow of the horizontal circulation are partially canceled along depth levels but not along density levels due to their different densities, as illustrated in the  $\sigma$ -z diagram (see “Methods”, Fig. 6d, e). We can roughly estimate the total horizontal circulation contribution to the maximum mean density-space AMOC across OSNAP East using the difference between the maximum mean density-space and depth-space AMOC (see “Methods”), which is 5.6Sv, 7.3Sv, 6.3Sv for the OSNAP observations, the RDC experiment, and the

control simulation respectively (Fig. 3b, e). Here a positive value corresponds to an increase in the density-space AMOC relative to the depth-space AMOC due to the contribution from the horizontal circulation across OSNAP East (Figs. 3b, e, 5). The above estimated total horizontal circulation contributions account for about 41%, 44%, 42% of the maximum mean density-space AMOC across OSNAP East (i.e., 13.8Sv, 16.5Sv, 14.9Sv) for the OSNAP observations, the RDC experiment, and the control simulation respectively. Such a contribution would be missing in 2-dim ocean models. The horizontal circulation contribution to the density-space AMOC is much smaller across OSNAP West than that across OSNAP East (Figs. 3, 6), also due to the much smaller density contrast between the Labrador Sea boundary inflow and outflow (Figs. 4, 5).

**The AMOC across the Arctic-Atlantic gateway sections.** The RDC experiment has a maximum mean AMOC of 6.3Sv at  $27.73\text{kg m}^{-3}$  (Fig. 7a) across the GSR, including a total of  $\sim 6.0\text{Sv}$  GSR overflow ( $\sigma_0 > 27.8 \text{ kg}^{-3}$ ):  $\sim 3.4\text{Sv}$  across the Denmark Strait (DS),  $\sim 0.5\text{Sv}$  across the Iceland-Faroe subsection, and  $\sim 2.1\text{Sv}$  across the Faroe-Scotland subsection, consistent with recent observations<sup>38-40</sup>. Further northeast across the section of FS and BSO, the RDC experiment exhibits a maximum mean AMOC of  $\sim 2.9\text{Sv}$  at  $28.0 \text{ kg m}^{-3}$ , whereas across the  $68^\circ\text{N}$  section the maximum mean AMOC is only  $\sim 3.7\text{Sv}$  at  $27.94 \text{ kg m}^{-3}$  and the southward transport denser than  $28.0 \text{ kg m}^{-3}$  is less than  $\sim 3.5\text{Sv}$  (Fig. 7a). Hence the region including the Greenland Sea between  $68^\circ\text{N}$  and the FS/BSO section (Fig. 1) contributes negligibly ( $\sim 0.6\text{Sv}$ ) to the southward downstream AMOC transport denser than  $28.0 \text{ kg m}^{-3}$  across  $68^\circ\text{N}$ , despite the presence of strong Greenland Sea deep convection (likely overestimated) in the RDC experiment (Supplementary Fig. 2a).

The relatively denser part ( $\sigma_0 > 28.0 \text{ kg m}^{-3}$ ) of the GSR overflow is dominated by the deep branch of the AMOC across the FS/BSO (Fig. 7a), indicating that the densification along the two branches of the Atlantic inflow to the Arctic through the BSO and east FS<sup>21-23</sup>, and associated Arctic transformed dense outflow through the FS<sup>21,23,41,42</sup> (Fig. 1), are important AMOC processes that provide the densest source water to the long-term mean AMOC strength.

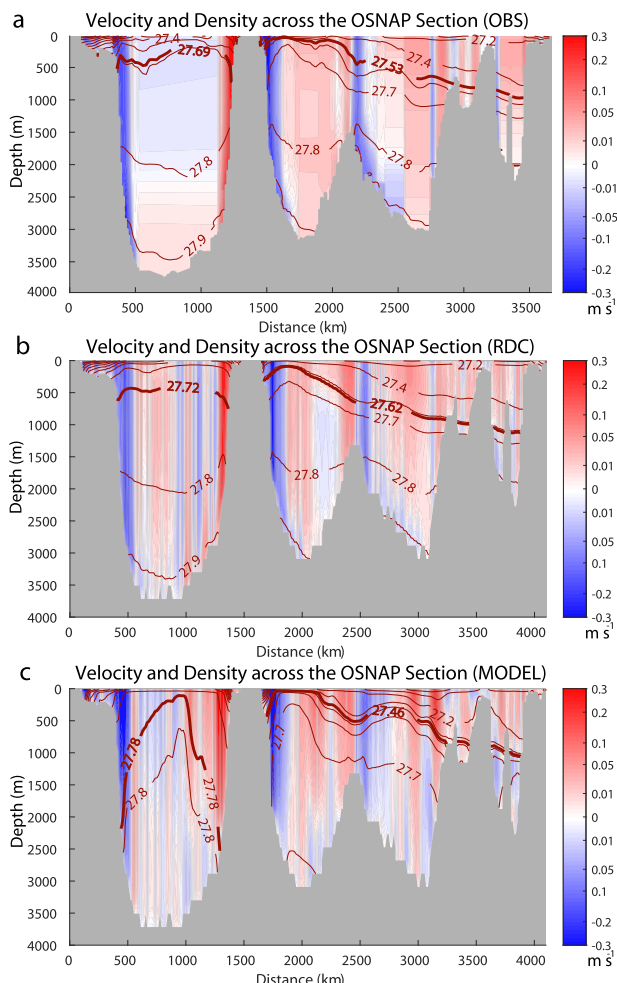


**Fig. 4 Mean velocity ( $\text{m s}^{-1}$ ) and potential density ( $\sigma_0, \text{kg m}^{-3}$ ) across the OSNAP section. a** OSNAP Observations (OBS). **b** Robust diagnostic calculation (RDC). **c** Control simulation (MODEL). The thick dark red isopycnals in (a-c) denote the density level at which the maximum mean AMOC occurs in each subsection (27.53, 27.69  $\text{kg m}^{-3}$  in OBS, 27.62, 27.72  $\text{kg m}^{-3}$  in RDC, and 27.46, 27.78  $\text{kg m}^{-3}$  in MODEL for OSNAP East, OSNAP West respectively). The contours are in increments of 0.2 (0.1)  $\text{kg m}^{-3}$  above (below) the thick isopycnals.

This is also consistent with the view that the near-boundary convection and associated shelf dense water formation in the Arctic could be important for the GSR overflow<sup>21,23</sup>. The less-dense part ( $27.8 \text{ kg m}^{-3} < \sigma_0 < 28.0 \text{ kg m}^{-3}$ ) of the GSR overflow is mainly supplied from the densification of the Atlantic inflow between 68°N and the GSR (Fig. 7a), where there is no deep convection (Supplementary Fig. 2a). The RDC experiment shows a southward subsurface outflow off the Norwegian slope (Fig. 8c) moving towards the Faroe Bank Channel (FBC), suggesting the newly observed eastern boundary pathway towards the FBC overflow<sup>43</sup> also exists in the long-term mean. The southward flow towards the FBC can be traced back to the region of the Vøring Plateau and is consistent with the long-term mean temperature/salinity/density structure in this region in the RDC experiment.

Across the above-mentioned sections, the maximum mean AMOC in depth-space is also smaller than that in density-space in the RDC experiment (Fig. 7a, c), suggesting that the horizontal circulation extending into the Nordic Seas (Fig. 2a, b) and flowing across sloping isopycnals (Fig. 8a, c, e) also contributes to the density-space AMOC (Fig. 7a, c). This horizontal circulation in the Nordic Seas is consistent with observational analyses: the

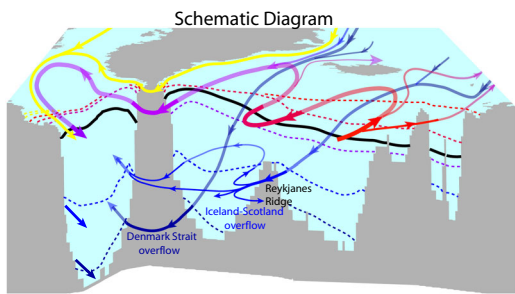


**Fig. 5 Schematic diagram (3-dim) of the AMOC across the OSNAP section and associated contribution to the density-space AMOC from the horizontal subpolar gyre circulation based on robust diagnostic calculation (RDC) results.** Colors of isopycnals (from RDC, dashed lines) and flow arrows indicate seawater density (light to dense: yellow-red-purple-violet-blue-dark blue). As in Fig. 1, the density of Atlantic inflow increases along the pathways of the cyclonic gyre. The black thick lines (isopycnals from RDC) denote the density level at which the maximum mean AMOC occurs in each subsection. Across OSNAP East, the lighter (denser) branch of the cyclonic gyre moves with a net northward (southward) transport above (below) the thick isopycnal, representing the important contribution of the horizontal subpolar gyre circulation to the density-space AMOC. The density contrast across OSNAP East is much larger than that across OSNAP West, consistent with a much stronger AMOC across OSNAP East than that across OSNAP West due to both thermal wind contribution and horizontal circulation contribution. Note only the upper ocean gyre is illustrated here as an example, but as shown in Fig. 4 the gyre also extends below the upper ocean.

Atlantic inflow enters the Nordic Seas mainly through the eastern GSR<sup>15,44</sup>, part of it recirculates and turns southward near the FS and along eastern Greenland<sup>22,24,45</sup>, and exits through the DS<sup>24,40,44</sup> (Fig. 1). The horizontal circulation contribution is consistent with the observation that the anomalous temperature/salinity of the DS overflow water is correlated and lags that of the recirculating Atlantic water near the FS and the Atlantic inflow water entering the Nordic Seas through the eastern GSR<sup>24</sup>. The horizontal circulation contribution to the AMOC is small across the FS/BSO and 68°N, but a bit larger across the GSR (Fig. 7a, c) due to a relatively larger density contrast between the inflow and outflow there (Fig. 8a, c, e, Supplementary Fig. 6a, c, e). All RDC experiments show similar results (Supplementary Fig. 7).

In the RDC experiment, the reduction of the maximum mean density-space AMOC across 68°N compared to that across the GSR (Fig. 7a) is due to both the reduction in the depth-space thermal wind contribution and the reduction in the horizontal circulation contribution (Fig. 7a, c); both are related to the relatively smaller density contrast across 68°N compared to that across the GSR (Fig. 8c, e), which sustains a relatively weaker AMOC across 68°N. The heat loss and densification along the Atlantic inflow pathway between the GSR and 68°N contributes to the relatively colder and denser Atlantic inflow across 68°N and the relatively smaller density contrast there compared to that across the GSR (Fig. 8c, e). Consistently, the maximum mean AMOC occurs at a much denser level across 68°N than that across the GSR (Figs. 7a, 8c, e). The densification process of the Atlantic inflow between the GSR and 68°N provides a major source for the less-dense part ( $27.8 \text{ kg m}^{-3} < \sigma_0 < 28.0 \text{ kg m}^{-3}$ ) of the GSR overflow and for the changes of the density-space AMOC between these two sections (Fig. 7a). The lower branch of the depth-space AMOC extends deeper across 68°N than that across the GSR (Fig. 7c) due to changes in the bathymetry (Fig. 8c, e).

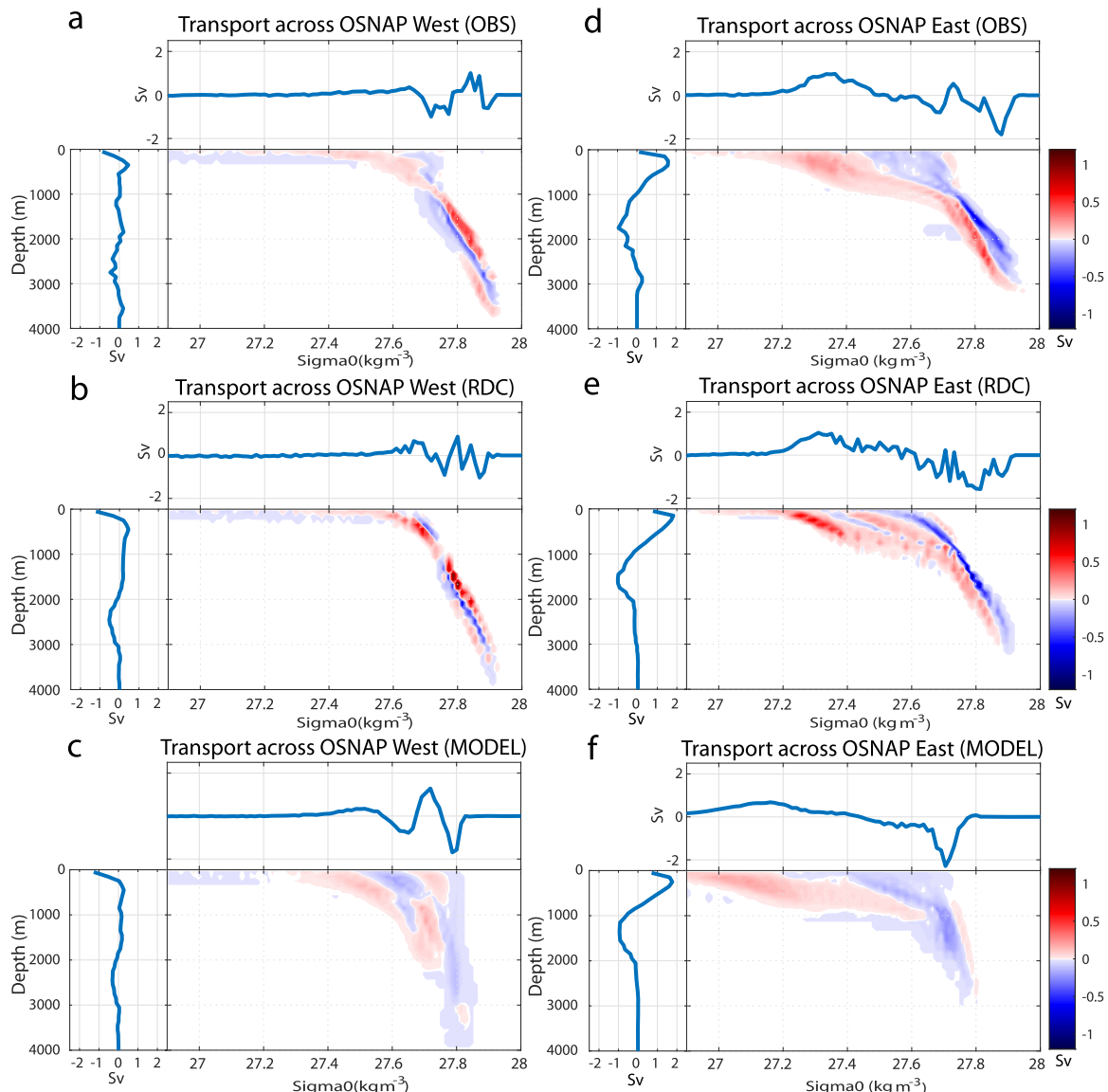


**Fig. 6 Mean  $\sigma$ -z diagram of AMOC transport (Sv) across OSNAP West and OSNAP East. a, d** OSNAP observations (OBS). **b, e** Robust diagnostic calculation (RDC). **c, f** Control simulation (MODEL). **a-c** OSNAP West subsection. **d-f** OSNAP East subsection. The color shaded  $\sigma$ -z diagram in each panel shows the integrated volume transport (Sv) across each subsection over each potential density ( $\sigma_0$ ) bin (x-axis) and depth (z) bin (y-axis); the integrated transport across each subsection over each potential density bin summed over the entire depth range is shown in the blue curve above; the integrated transport across each subsection at each depth bin summed over the entire potential density range is shown in the blue curve on the left. The accumulated AMOC transport in density- and depth- space corresponds to AMOC streamfunctions across each subsection (Fig. 3a, b, d, e).

In the control simulation, the deep AMOC branch across the FS/BSO also provides the densest source water to the AMOC and dominates the relatively denser part of the GSR overflow, although the AMOC across all Arctic-Atlantic gateway sections shifts to lower densities due to model biases (Figs. 7b, 8b, d, f, Supplementary Fig. 6b, d, f). The region between 68°N and the FS/BSO section in the control simulation has a biased larger contribution to the southward density-space AMOC transport across 68°N mainly due to a biased larger horizontal circulation contribution (Fig. 7b, d) (see “Methods”), despite the lack of simulated Greenland Sea deep convection (Supplementary Fig. 2b).

### Conclusion and discussion

Our RDC results show that the deep AMOC branch across the FS/BSO (i.e., the Arctic outflow) provides the densest source water to the mean AMOC. The Arctic Ocean, not the Greenland Sea, is the

northern terminus of the mean AMOC, i.e., the maximum mean AMOC (~2.9Sv) across the FS/BSO and associated densification processes through the Barents Sea and the Arctic are part of the long-term mean AMOC structure. The heat loss contributes to the densification/transformation of the Atlantic inflow in the Nordic Seas<sup>46</sup>, but not all the dense Atlantic inflow water transformed within the Nordic Seas directly returns southward there. We show that a little less than half (i.e., ~2.9Sv) of the dense Atlantic inflow water transformed in the Nordic Seas continues to move eastward and northward into the Barents Sea and the Arctic, and gets further transformed and becomes denser in the Barents Sea and in the Arctic before it returns southward as the Arctic outflow and contributes to the densest part of the GSR overflow. Hence the most northeastern part of the long-term mean AMOC is not confined by the Nordic Seas and does not terminate at the northern and eastern boundary of the Nordic Seas. The heat loss over the shallow Barents Sea is effective for the densification of the

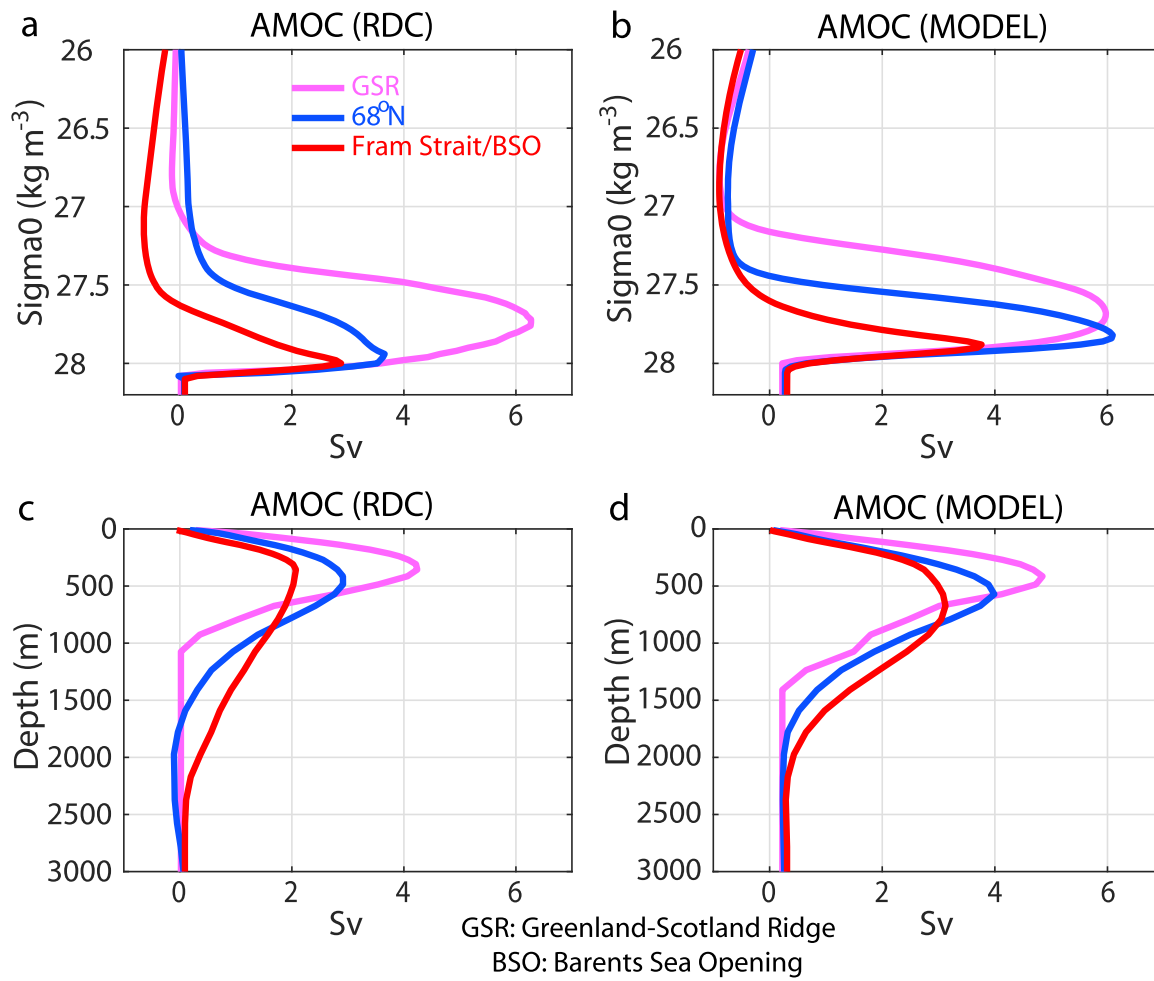


**Fig. 7 Mean AMOC streamfunctions across Arctic-Atlantic Gateways sections (shown in Fig. 1). a, b** Density-space ( $\sigma_0$ ,  $\text{kg m}^{-3}$ ). **c, d** Depth-space (m). **a, c** Robust diagnostic calculation (RDC). **b, d** Control simulation (MODEL). Red: Section across Fram Strait (FS)/Barents Sea Opening (BSO); Blue: Section across 68°N in Nordic Seas. Pink: Section across Greenland-Scotland Ridge (GSR, including English Channel).

Atlantic inflow<sup>47</sup>, and the near-boundary convection and associated shelf dense water formation in the Arctic could be important for the transformation of the Atlantic inflow entering the Arctic<sup>21,23</sup>. The modeled low-density biases in the deep AMOC branch across all Arctic-Atlantic gateways sections in the control simulation could be traced back to the modeled low-density biases in the Arctic outflow, indicating the model's deficiency in simulating the densification processes in the Arctic.

We also show that open-ocean deep convection in either the Labrador or Greenland Seas contributes minimally to the long-term mean AMOC strength. Hence a shutdown of open-ocean deep convection in the Labrador and Greenland Seas would not necessarily weaken the AMOC substantially, even though it would significantly reduce deep ocean ventilation<sup>36,48</sup>. Climate models often overestimate the mean AMOC across the Labrador Sea<sup>49,50</sup>, likely due to too broad boundary outflow overlapping with an interior high-density deep convection region in coarse-resolution models, and/or unrealistically high-density contrasts between the boundary inflow and outflow. It is important for climate models to resolve realistic boundary currents and simulate a faithful long-term mean boundary inflow and outflow density contrast and associated AMOC structure to avoid overpredictions of the role of open-ocean deep convection in future AMOC changes.

After the dense GSR overflow passes through the DS and FBC, the entrainment processes associated with the substantial deepening in the bathymetry<sup>9,39</sup> contribute to the lighter, deeper, and

stronger downstream AMOC outflow across OSNAP East (Figs. 3b, e, 7a, c). The heat loss/densification of the Atlantic inflow between OSNAP East and the GSR contributes to a denser AMOC inflow across the GSR than that across OSNAP East (Figs. 3b, 4b, 7a, 8e). In the RDC experiment, the increase of the maximum long-term mean AMOC across OSNAP East compared to that across the GSR is much larger in density-space (10.2Sv, i.e. from 6.3Sv across the GSR to 16.5Sv across OSNAP East) than in depth-space (4.9Sv, i.e., from 4.3Sv across the GSR to 9.2Sv across OSNAP East) (Figs. 3b, e, 7a, c). The northeastern subpolar North Atlantic has been identified as a key region for the AMOC over the recent OSNAP period<sup>46</sup>. The RDC results suggest that this region is also important for the long-term mean AMOC over the past several decades. The heat loss/densification of the horizontal circulation (the northeastern subpolar gyre, the gyre extended into Nordic Seas, and the branches entering the Arctic through FS/BSO) along its pathways contributes to the long-term mean density-space AMOC (Figs. 1, 5). Over the northeastern subpolar North Atlantic, the horizontal circulation moving across sloping isopycnals has increased substantially from that over the Nordic Seas (Fig. 2b). This horizontal circulation and associated densification process along its cyclonic pathways (Figs. 1, 5) also contribute to the much stronger long-term mean density-space AMOC across OSNAP East compared to that across the GSR (Figs. 3b, 7a), in addition to the contribution from the entrainment processes.

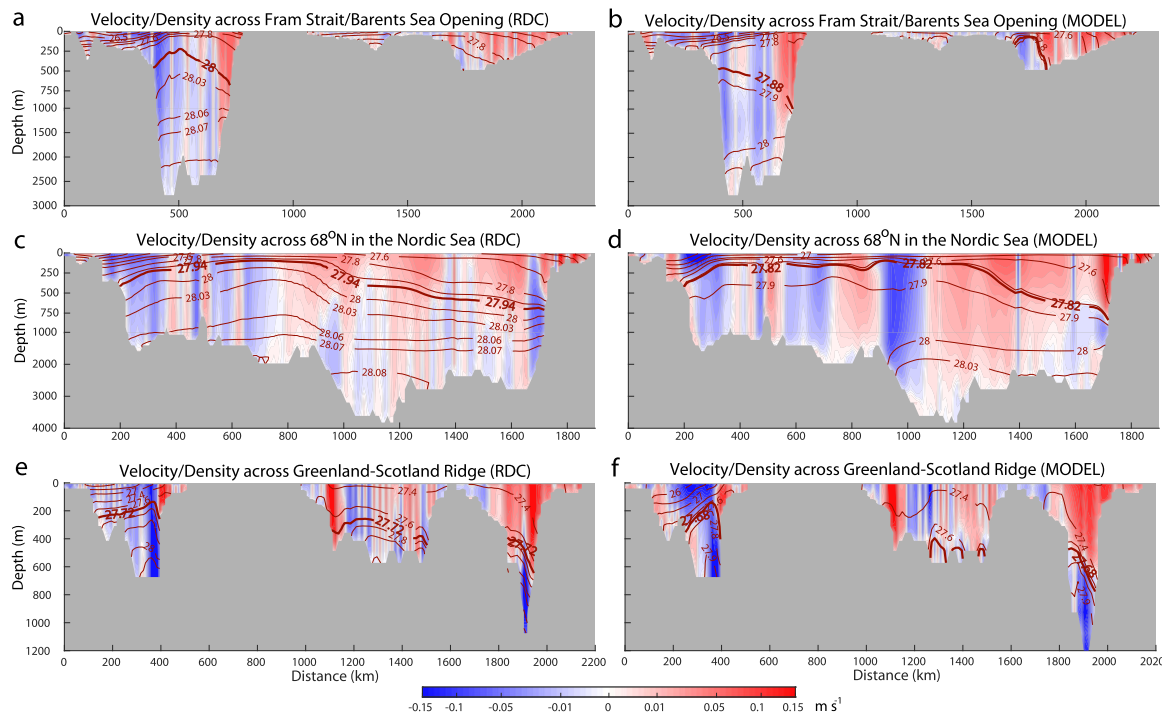


**Fig. 8 Mean velocity ( $\text{m s}^{-1}$ ) and potential density ( $\sigma_0, \text{kg m}^{-3}$ ) across Arctic-Atlantic Gateways sections (shown in Fig. 1). a, c, e** Robust diagnostic calculation (RDC). **b, d, f** Control simulation (MODEL). **a, b** Section across the Fram Strait (FS) and Barents Sea Opening (BSO). **c, d** Section across  $68^\circ\text{N}$  in the Nordic Seas. **e, f** Section across the Greenland-Scotland Ridge (GSR, including English Channel). Thick dark red isopycnals denote the density level at which the maximum mean AMOC occurs in each section (28.0, 27.94, 27.72  $\text{kg m}^{-3}$  in RDC, and 27.88, 27.82, 27.68  $\text{kg m}^{-3}$  in MODEL for FS/BSO,  $68^\circ\text{N}$ , GSR respectively). The upper 1000 m in (a-d) is expanded.

Across OSNAP East, the density contrast is much larger than that across OSNAP West, sustaining a much larger AMOC than that across OSNAP West through both thermal wind contribution and horizontal circulation contribution. This result holds over the past several decades, not just over the recent OSNAP period. Our analyses show that the horizontal circulation across sloping isopycnals contributes substantially (more than 40%) to the mean northeastern subpolar AMOC and provides an additional important physical mechanism for why the AMOC is much larger across OSNAP East than that across OSNAP West (Fig. 5). As discussed earlier in the comparison with additional RDC experiments, a lower upper-ocean salinity/density along the EGC (Supplementary Fig. 3) could reduce the density contrast and result in a weaker AMOC across the OSNAP section/OSNAP East (Supplementary Fig. 4). The Great Salinity Anomaly events with reduced upper-ocean salinity/density along the boundary outflow (e.g., EGC)<sup>51,52</sup> might have weakened the AMOC directly through reduced density contrast and contributed to multidecadal AMOC variability, even if they had not affected interior Labrador or Greenland Seas deep convection. In the control simulation, the low-frequency variability of the maximum density-space AMOC across the OSNAP section is highly correlated with the component across OSNAP East and its horizontal circulation contribution (Supplementary Fig. 8), and not with that across OSNAP West or the variations of deep convection in the Labrador and Greenland Seas.

The maximum mean AMOC across OSNAP East, from recent OSNAP observations is weaker than the maximum long-term mean AMOC estimated from the RDC experiment (Fig. 3). The difference in their Ekman components is negligible. This weakening (in the non-Ekman component) might be related to a slight lower salinity/density anomaly along the EGC ( $\Delta S \approx -0.54 \text{ PSU}$ ;  $\Delta \sigma_0 \approx -0.35 \text{ kg m}^{-3}$  at 100 m) and a slight colder/denser anomaly along the interior inflow (Fig. 4a, b, Supplementary

Fig. 5b, d); thus a slightly reduced density contrast and a slight shift of the upper-ocean outflow to lower densities across OSNAP East (Fig. 6d, e) over the recent OSNAP period (2014–2016), compared to the long-term mean. Interestingly, estimates of the maximum mean AMOC across a nearby section ( $59.5^\circ\text{N}$  Greenland to Scotland) during the early 2000s (16.5Sv)<sup>12</sup> and over the satellite period (17.4Sv)<sup>14</sup> are similar to that estimated from the RDC experiment (16.5Sv) across the same  $59.5^\circ\text{N}$  section and across OSNAP East. More investigations would be needed to understand and verify whether the relatively weaker AMOC across OSNAP East observed during the recent OSNAP period (2014–2016) persists. Future AMOC changes across a northern section might be closely related to future changes of the density contrast between the inflow and outflow and/or future changes in the strength of the horizontal circulation across that section. Even if the GSR overflow remains stable as observed over the last two decades<sup>39,40</sup>, it is still possible to have a weaker northeastern subpolar AMOC if the upper-ocean density contrast across the northeastern subpolar basin decreases in the future.

The RDC experiment, using a high-resolution global coupled climate model in conjunction with the observed full-depth hydrographic climatology, is not only consistent with key observed AMOC characteristics at existing AMOC sections (e.g., OSNAP), but also provides a holistic long-term mean AMOC structure over the extratropical North Atlantic and the Arctic Mediterranean, including long-term mean AMOC structure across some un-monitored Arctic-Atlantic gateways sections (e.g.,  $68^\circ\text{N}$  in the Nordic Seas). The RDC results suggest that the Arctic Mediterranean and the northeastern subpolar North Atlantic are key regions for the long-term mean AMOC. Open-ocean deep convection in either the Labrador or Greenland Seas contributes minimally to the long-term mean AMOC strength. The densification along the full extent of the AMOC inflow all the way into the Arctic (i.e., the northern terminus of the mean AMOC), and

the associated contribution of the horizontal circulation across sloping isopycnals are important for the long-term mean AMOC. The Arctic outflow through the FS provides the densest source water to the long-term mean AMOC. The newly observed interior Iceland-Scotland overflow pathways<sup>31</sup> and the eastern boundary pathway towards the FBC overflow<sup>43</sup> also exist in the long-term mean. This long-term mean AMOC structure at northern high latitudes will be valuable in guiding modeling/observational efforts for predicting/detecting future AMOC changes.

## Methods

**RDC experiments and associated long-term mean hydrographic data.** The RDC experiments conducted in this study provide an observational-based estimate of the long-term mean AMOC structure at northern high latitudes over the past several decades.

The main focus region of this study is the extratropical North Atlantic and the Arctic Mediterranean. To obtain an approximation of realistic ocean circulation in this region, the restoring of model potential temperature and salinity to the observed hydrographic climatology is very strong with a time scale of 5 days over the extratropical North Atlantic (i.e., north of 30°N) and the Arctic Mediterranean (including the Arctic Ocean and marginal seas such as the Barents Sea and the Nordic Seas). Hence the model potential temperature and salinity are very close to the observed hydrographic climatology in this region. Outside the above focus region, especially over the tropical Atlantic, the restoring is less strong with a time scale of 2 years to avoid unrealistic ocean circulation near the equator where the Coriolis parameter disappears and thus the geostrophic balance breaks down. If the restoring time scale is <2 years, there is a strong unrealistic anti-clockwise deep ocean overturning circulation near the equator. Over the connecting region between the tropical and extratropical North Atlantic (i.e., between 15°N and 30°N in the North Atlantic), the restoring time scale is 180 days. The same 2-year restoring time scale is also applied to the entire South Atlantic and other ocean basins outside the Atlantic and the Arctic Mediterranean for simplicity.

One key observed long-term mean hydrographic data used in this study is the World Ocean Atlas 2013 (WOA13) version 2 with objectively analyzed climatological fields of monthly mean in situ temperature<sup>53</sup> and salinity<sup>54</sup> averaged for the period 1955–2012 on a 1/4° horizontal grid and 102 vertical levels. The data cover full depth (from ocean surface to ocean bottom) over the global ocean domain. It includes the seasonal cycle of temperature and salinity fields above 1500 m and the annual mean fields below 1500 m. Among the 102 vertical levels, 57 levels are above 1500 m and 45 levels are below 1500 m. Another key observed long-term mean hydrographic data used in this study is the climatology of seasonal ocean hydrographic properties developed and provided by the Commonwealth Scientific and Industrial Research Organisation (CSIRO) Marine and Atmospheric Research<sup>55,56</sup>, i.e., CSIRO ATLAS of REGIONAL SEAS 2009 version (CARS2009). The long-term mean temperature and salinity fields in CARS2009 cover the full global oceans on a 1/2° horizontal grid and 79 vertical levels. The data also cover full depth over the global ocean domain. They are created by averaging/interpolating all available oceanographic profile data, most of which were collected in the last 50 years (e.g., World Ocean Database 2005 updated to July 2008, Argo up to May 2009, WOCE Global Hydrographic Program (v3.0), and many other datasets available up to 2008). It includes the seasonal cycle of temperature and salinity fields above 1800 m and the annual mean fields below 1800 m, due to the substantially enhanced observations that are available to provide the seasonal cycle information in the upper ocean. Among the 79 vertical levels, 64 levels are above 1800 m and 15 levels are below 1800 m. The relatively high vertical resolution of the hydrographic data in the upper ocean also reflects the fact that there are much more observational data in the upper ocean than in the deep ocean. CARS2009 employs extra stages of in-house quality control of input data and is designed to provide an estimate of ocean properties at each grid that is faithful to the data. Both the WOA13 and the CARS2009 datasets are regridded onto the high-resolution global coupled climate model's ocean grid with a 1/4° horizontal resolution and 50 vertical levels and interpolated at each model time step with a repeated annual cycle, and the in situ temperature data are converted into the potential temperature data before the regridding.

The main reason that CARS2009 is employed in this study in addition to WOA13 is that CARS2009 can resolve the cold fresh upper-ocean properties along the East Greenland Current (EGC) better than WOA13 (Supplementary Fig. 3), especially near the western boundary of the Overturning in the Subpolar North Atlantic Program (OSNAP) EAST subsection around the tip of Greenland. In the real world, the density along the cold fresh EGC is less sensitive to cold temperature and strongly affected by its relatively low salinity, which gives rise to a lower density than that along the nearby Irminger Current. The light (cold fresh) upper-ocean properties along the EGC, which can also be seen from OSNAP observations (Fig. 4a, Supplementary Fig. 5a, b), are not well resolved in WOA13, resulting in an inaccurately higher surface salinity/density there in WOA13 than in CARS2009 (Supplementary Fig. 3). However, WOA13 is widely used and has similar ocean properties in general as CARS2009 but with higher horizontal and vertical resolutions. For these reasons, in the RDC experiment shown in the main

paper, the model potential temperature and salinity are restored to a combined observed hydrographic climatology, i.e., the CARS2009 data in the Atlantic and the Nordic Seas, and the WOA13 data in all other ocean regions, to achieve a more accurate result.

In the RDC experiment shown in the main paper, to have an accurate estimate of the Ekman component of the AMOC (i.e., the integrated Ekman transport across a section), the surface wind stress is overridden and prescribed everywhere over the global ocean with the climatological monthly mean surface zonal and meridional wind stress averaged for the period 1979–2018 from the ERA-Interim reanalysis data<sup>57</sup>.

Two additional RDC experiments have been conducted for comparisons and the results are shown in Supplementary Fig. 4: (1) the RDC experiment using the WOA13 data everywhere in the global ocean and with surface wind stress overriding using the same ERA-Interim surface wind stress climatology, referred to as RDC/WOA; (2) the RDC experiment using the WOA13 data everywhere in the global ocean and No surface Wind stress Overriding (i.e., the surface wind stress is simulated by the coupled model itself), referred to as RDC/WOA/NWO. All RDC experiments are run for 80 years. The solution reaches a quasi-equilibrium state within a decade. To avoid the initial spin-up period, we use the average of the last 60 years as the corresponding climatological mean for each RDC experiment.

In RDC/WOA, because the WOA13 data do not resolve well the low salinity/density along the EGC (Supplementary Fig. 3), the AMOC across OSNAP East and the entire OSNAP section is stronger (Supplementary Fig. 4) than that in the RDC experiment shown in the main paper (using the CARS2009 data in this region). Nevertheless, the main results reported in this study hold for all RDC experiments using different observed long-term mean hydrographic data in the Atlantic and the Nordic Seas, and are not sensitive to the inclusion of surface wind stress overriding.

**Model and present-day control simulation.** A high-resolution global coupled climate model, Geophysical Fluid Dynamics Laboratory (GFDL) coupled climate model version 2.5 (CM2.5)<sup>29</sup>, is employed in this study. The atmospheric component has 32 levels in the vertical and ~50 km in the horizontal. The ocean component has 50 vertical levels and an eddy-permitting (1/4°) horizontal resolution varying from ~27.75 km at the equator to ~9 km at high latitudes with a squared isotropic grid. In this study, a new present-day control simulation under the 1990 radiative forcing conditions is conducted with this model for 200 years. The 80-year RDC experiments are also conducted with this model under the same 1990 radiative forcing conditions. In the RDC experiments and the 200-year control simulation, the ocean bathymetry is modified from the original model bathymetry. For example, with the original bathymetry used in CM2.5<sup>29</sup>, the Faroe Bank Channel (FBC) overflow is not well resolved and the Denmark Strait (DS) has been deepened to 850 m to strengthen the DS overflow, thus the DS overflow dominates the total Nordic Seas overflow. In the RDC experiments and the 200-year control simulation used in this study, to avoid the artificial strengthening of the DS transport and achieve a better resolved FBC overflow and a more realistic distribution among DS and FBC transports, the bathymetry around Faroe has been deepened by 300 m and the DS has been set to have a realistic depth of ~616 m instead of the artificially deepened depth (850 m) used in the original model bathymetry. The area of deepening around Faroe is smaller in the RDC experiments than that in the control simulation because the RDC experiments can achieve a better distribution among DS and FBC transports. To avoid the impact of the initial spin-up, we use the average of the last 60 years of the 200-year control simulation as the climatological mean for the control simulation. In both the RDC and the control simulation, the mixed layer depth (mld) is derived from the online mld output calculated using the standard CM2.5 diagnostics<sup>58</sup> with a buoyancy criterion of 0.0003 ms<sup>-2</sup>.

**The  $\sigma$ -z diagram of AMOC transport.** In this study, a  $\sigma$ -z diagram is designed for the first time to illustrate the horizontal circulation contributions to the AMOC in density-space at each depth across a section. The  $\sigma$ -z diagram is derived from monthly mean data, i.e., the monthly mean volume transport (Sv) perpendicular to the section at each grid location across the section  $T(x, y, z, t)$  is categorized into equally spaced potential density bins  $T_C(x, y, \sigma_0, z, t)$  based on the corresponding monthly mean potential density at the location  $\sigma_0(x, y, z, t)$ , and summed over the section as a function of potential density and depth,  $T_S(\sigma_0, z, t)$ , then averaged over time, i.e.,  $T_{S, Mean}(\sigma_0, z) = \overline{T_S(\sigma_0, z, t)}$ . The volume transport on the model depth interval is normalized to equal depth bins. The bin sizes are 100 m and 0.0136 kg m<sup>-3</sup> respectively. The color shading in the  $\sigma$ -z diagram represents the integrated volume transport across a section over each potential density ( $\sigma_0$ ) bin (x-axis) and depth (z) bin (y-axis). The volume transport across a section at each potential density bin summed over the entire depth range can be found in the curve above the  $\sigma$ -z diagram. The volume transport across a section at each depth bin summed over the entire potential density range can be found in the curve on the left of the  $\sigma$ -z diagram. The accumulated volume transport in density- or depth-space corresponds to the AMOC streamfunctions across the section in density- or depth-space respectively. The volume transport within certain ranges of depth and potential density can also be summed from the  $\sigma$ -z diagram. The  $\sigma$ -z diagram illustrates where and how much of the horizontal circulation contribution to the AMOC across a section is canceled in depth-space but visible in density-space if

isopycnals across the horizontal circulation are tilted in depth-space (i.e., if the inflow and outflow of the horizontal circulation are associated with different densities).

**Comparisons with the satellite observed mean dynamic topography.** We compared the global and regional spatial maps of the climatological mean SSH from the RDC experiment and the control simulation with the independent satellite observed  $\frac{1}{4}$ ° climatological mean dynamic topography, i.e., the 20-year (1993–2012) mean SSH above geoid<sup>59</sup> distributed by Aviso+. The climatological mean SSH from the RDC experiment compares very well with the independent satellite observed mean dynamic topography over the extratropical North Atlantic and the Nordic Seas (Fig. 2a, b) as well as over the entire global ocean (Supplementary Fig. 1a, b). The mean SSH from the RDC experiment is a bit smoother than that from the satellite observation (e.g., the anti-cyclonic Mann eddy adjacent to the NAC pathway is less pronounced) (Fig. 2a, b), likely because the RDC experiment represents a mean state over a much longer period (past several decades) than the satellite period. The control simulation exhibits some typical deficiencies found in many climate models, e.g., the Gulf Stream and NAC pathways (Fig. 2c), but produces reasonable results over most ocean basins (Supplementary Fig. 1c).

**Comparisons with observations across the OSNAP section.** We compared the climatological mean AMOC stream functions, velocity, density, and the  $\sigma$ -z diagram across the OSNAP East and West subsections from the RDC experiment and the control simulation with the 21-month mean OSNAP observations<sup>16,60,61</sup>. In both the RDC experiment and the control simulation, the net southward transport across the entire OSNAP section (Fig. 3c, f) reflects the continuous net southward transport of cold fresh water across the Davis Strait<sup>62</sup> and OSNAP West (Fig. 3a, d), which is consistent with the surface freshwater flux in the fully coupled framework. Hence we chose not to adjust the net transport across OSNAP East to compensate for the OSNAP West southward transport to achieve a zero net transport across the entire OSNAP section in the RDC experiment and the control simulation, although the observed transport data across OSNAP East do include an adjustment to achieve a zero net transport across the entire OSNAP section<sup>16</sup>. This minor difference does not affect the conclusions of this study. Note that the maximum of the mean AMOC (which is focused on in this study) is different from the mean of the maximum AMOC, since the density level at which the maximum AMOC occurs changes over time<sup>16</sup>. The Ekman component of the AMOC for the OSNAP observations<sup>16</sup>, the RDC experiment, and the control simulation is about  $-1.5\text{Sv}$ ,  $-1.3\text{Sv}$ , and  $-0.7\text{Sv}$  (southward) respectively across OSNAP East, and negligible across OSNAP West.

We use the difference between the maximum mean AMOC in density-space and depth-space across OSNAP East as a rough estimate of the total horizontal circulation contribution to the maximum mean AMOC in density-space across this subsection, because the deepest depth of the isopycnal ( $\sigma_0^{\text{max}}$ ) at which the maximum mean density-space AMOC occurs (Fig. 4) is similar to the depth level ( $z^{\text{max}}$ ) at which the maximum depth-space mean AMOC occurs (Fig. 3e) across this subsection. That is, across OSNAP East, the maximum mean density-space AMOC roughly corresponds to the net integrated northward volume transport above this isopycnal ( $\sigma_0^{\text{max}}$ ), and the maximum mean depth-space AMOC corresponds to the net integrated northward volume transport above this depth level ( $z^{\text{max}}$ ) (Fig. 4). Hence, the difference between the maximum mean AMOC in density-space and depth-space across OSNAP East corresponds roughly to the net integrated southward volume transport enclosed by the region below this isopycnal ( $\sigma_0^{\text{max}}$ ) and above this depth level ( $z^{\text{max}}$ ) (Fig. 4). This difference represents roughly the total horizontal circulation contribution to the maximum mean AMOC in density-space across this subsection and is cancelled in depth-space by part of the net integrated northward transport above this isopycnal ( $\sigma_0^{\text{max}}$ ).

**AMOC biases in the control simulation.** In the control simulation, the AMOC across the OSNAP section/OSNAP East is shallower and shifts to lower densities (Fig. 3b, c, e, f). This modeling bias is related to excessive numerical diapycnal mixing of the overflows south of the GSR, a typical issue in climate models with a depth-coordinate ocean component<sup>31,63,64</sup>. This is also related to the modeling bias that the deep AMOC branch across the FS/BSO section and thus across all Arctic-Atlantic gateways sections shifts to lower densities (Fig. 7b), indicating the model's deficiency in simulating the densification processes in the Arctic. The modeled horizontal circulation contribution to the density-space AMOC also shifts to lower densities and it is not well simulated below the upper ocean, as illustrated in the  $\sigma$ -z diagram (Fig. 6c, f).

In the control simulation, the stronger AMOC across  $68^{\circ}\text{N}$  compared to that in the RDC experiment (Fig. 7) is due to modeling biases, principally that the isopycnals near the eastern basin are too steep, the associated Norwegian Atlantic Slope Current off west-Norway is too strong, and the interior Norwegian Atlantic Front Current shifts too far east; there is an unrealistic density gradient and associate vertical shear and southward outflow in the middle of the basin (Fig. 8d, Supplementary Fig. 6d), an unrealistic eastward shift of the horizontal circulation in the Nordic Seas (Fig. 2c), and the horizontal circulation contribution to the AMOC in density-space is overestimated (Fig. 7b, d).

## Data availability

The World Ocean Atlas 2013 (WOA13) data were downloaded from the NOAA National Centers for Environmental Information (formerly the National Oceanographic Data) <https://www.nodc.noaa.gov/cgi-bin/OC5/woa13/woa13.pl>. The CSIRO ATLAS of REGIONAL SEAS 2009 version (CARS2009) data (<http://www.marine.csiro.au/~dunn/cars2009/>) were developed and provided by the Commonwealth Scientific and Industrial Research Organisation (CSIRO) Marine and Atmospheric Research, and downloaded from <http://www.marine.csiro.au/atlas/>. The climatological surface wind stress data are from the European Centre for Medium-range Weather Forecast (ECMWF): The ERA-Interim reanalysis data, Copernicus Climate Change Service (C3S) (accessed September 18, 2019), available from: <https://www.ecmwf.int/en/forecasts/datasets/archive-datasets/reanalysis-datasets/era-interim>. The observed mean dynamic topography data were produced by CLS and distributed by Aviso+ with support from Cnes (<https://www.aviso.altimetry.fr>), and downloaded from [ftp://ftp-access.aviso.altimetry.fr/auxiliary/mdt/mdt\\_cnes\\_cls2013\\_global/](ftp://ftp-access.aviso.altimetry.fr/auxiliary/mdt/mdt_cnes_cls2013_global/). Data from the full OSNAP (Overturning in the Subpolar North Atlantic Program) array for the first 21 months (31-Jul-2014 to 20-Apr-2016) were downloaded from <https://www.o-snap.org/>. OSNAP data were collected and made freely available by the OSNAP project and all the national programs that contribute to it ([www.o-snap.org](http://www.o-snap.org)). Other key data used in this study is available from <https://doi.org/10.5281/zenodo.4592442><sup>65</sup>.

## Code availability

The code of the Geophysical Fluid Dynamics Laboratory (GFDL) coupled climate model version 2.5 (CM2.5) is publicly available at <https://www.gfdl.noaa.gov/cm2-5-and-flor-quickstart/>.

Received: 4 January 2021; Accepted: 7 May 2021;

Published online: 08 June 2021

## References

1. Broecker, W. S., Petet, D. M. & Rind, D. Does the ocean-atmosphere system have more than one stable mode of operation? *Nature* **315**, 21–26 (1985).
2. Manabe, S. & Stouffer, R. J. Coupled ocean-atmosphere model response to freshwater input: comparison to Younger Dryas event. *Paleoceanography* **12**, 321–336 (1997).
3. Rahmstorf, S. Ocean circulation and climate during the past 120,000 years. *Nature* **419**, 207–214 (2002).
4. Zhang, R. et al. A review of the role of the Atlantic Meridional Overturning Circulation in Atlantic multidecadal variability and associated climate impacts. *Rev. Geophys.* **57**, 316–375 (2019).
5. Caesar, L., Rahmstorf, S., Robinson, A., Feulner, G. & Saba, V. Observed fingerprint of a weakening Atlantic Ocean overturning circulation. *Nature* **556**, 191–196 (2018).
6. Chen, X. & Tung, K. K. Global surface warming enhanced by weak Atlantic overturning circulation. *Nature* **559**, 387–391 (2018).
7. Brodeau, L. & Koenigk, T. Extinction of the northern oceanic deep convection in an ensemble of climate model simulations of the 20th and 21st centuries. *Clim. Dynamics* **46**, 2863–2882 (2016).
8. Heuzé, C. North Atlantic deep water formation and AMOC in CMIP5 models. *Ocean Sci.* **13**, 609–622 (2017).
9. Dickson, R. R. & Brown, J. The production of North Atlantic deep water: sources, rates and pathways. *J. Geophys. Res.: Oceans* **99**, 12319–12342 (1994).
10. Dengler, M., Fischer, J., Schott, F. A. & Zantopp, R. Deep Labrador Current and its variability in 1996–2005. *Geophys. Res. Lett.* **33**, 1–5 (2006).
11. Pickart, R. S. & Spall, M. A. Impact of Labrador Sea convection on the North Atlantic meridional overturning circulation. *J. Phys. Oceanogr.* **37**, 2207–2227 (2007).
12. Sarafanov, A. et al. Mean full-depth summer circulation and transports at the northern periphery of the Atlantic Ocean in the 2000s. *J. Geophys. Res.: Oceans* **117**, 1–22 (2012).
13. Holte, J. & Straneo, F. Seasonal overturning of the Labrador Sea as Observed by Argo Floats. *J. Phys. Oceanogr.* **47**, 2531–2543 (2017).
14. Rossby, T., Reverdin, G., Chafik, L. & Søiland, H. A direct estimate of poleward volume, heat, and freshwater fluxes at  $59.5^{\circ}\text{N}$  between Greenland and Scotland. *J. Geophys. Res.: Oceans* **122**, 5870–5887 (2017).
15. Chafik, L. & Rossby, T. Volume, heat, and freshwater divergences in the subpolar North Atlantic suggest the Nordic seas as key to the state of the meridional overturning circulation. *Geophys. Res. Lett.* **46**, 4799–4808 (2019).
16. Lozier, M. S. et al. A sea change in our view of overturning in the subpolar North Atlantic. *Science* **363**, 516–521 (2019).

17. Zou, S., Lozier, M. S., Li, F., Abernathay, R. & Jackson, L. Density-compensated overturning in the Labrador Sea. *Nat. Geosci.* **13**, 121–126 (2020).

18. Lumpkin, R. & Speer, K. Large-scale vertical and horizontal circulation in the North Atlantic Ocean. *J. Phys. Oceanogr.* **33**, 1902–1920 (2003).

19. Olsson, K. A. et al. Intermediate water from the Greenland Sea in the Faroe Bank Channel: spreading of released sulphur hexafluoride. *Deep-Sea Res. Part I* **52**, 279–294 (2005).

20. Brakstad, A., Våge, K., Håvik, L. & Moore, G. W. K. Water mass transformation in the Greenland Sea during the period 1986–2016. *J. Phys. Oceanogr.* **49**, 121–140 (2019).

21. Rudels, B. The thermohaline circulation of the Arctic Ocean and the Greenland Sea. *Philos. Trans. R. Soc. A: Phys. Eng. Sci.* **352**, 287–299 (1995).

22. Mauritzen, C. Production of dense overflow waters feeding the North Atlantic across the Greenland-Scotland Ridge. Part 1: Evidence for a revised circulation scheme. *Deep-Sea Res. Part I* **43**, 769–806 (1996).

23. Rudels, B., Quadfasel, D. & Friedrich, H. The Arctic Ocean Deep Water component in the Greenland-Scotland overflow. *ICES Cooperative Res. Rep.* **225**, 172–194 (1998).

24. Eldevik, T. et al. Observed sources and variability of Nordic seas overflow. *Nat. Geosci.* **2**, 406–410 (2009).

25. Sarmiento, J. L. & Bryan, K. An ocean transport model for the North Atlantic. *J. Geophys. Res.: Oceans* **87**, 394–408 (1982).

26. Wright, D. G., Thompson, K. R. & Lu, Y. Assimilating long-term hydrographic information into an eddy-permitting model of the North Atlantic. *J. Geophys. Res.: Oceans* **111**, 1–16 (2006).

27. Lee, S. K. et al. Global meridional overturning circulation inferred from a data-constrained ocean & sea-ice model. *Geophys. Res. Lett.* **46**, 1521–1530 (2019).

28. Zhang, R. & Vallis, G. K. The role of bottom vortex stretching on the path of the North Atlantic western boundary current and on the northern recirculation gyre. *J. Phys. Oceanogr.* **37**, 2053–2080 (2007).

29. Delworth, T. L. et al. Simulated climate and climate change in the GFDL CM2.5 high-resolution coupled climate model. *J. Climate* **25**, 2755–2781 (2012).

30. Zhang, R. Coherent surface-subsurface fingerprint of the Atlantic meridional overturning circulation. *Geophys. Res. Lett.* **35**, L20705 (2008).

31. Zhang, R. et al. Sensitivity of the North Atlantic Ocean circulation to an abrupt change in the Nordic Sea overflow in a high resolution global coupled climate model. *J. Geophys. Res.: Oceans* **116**, 1–14 (2011).

32. Menary, M. B., Jackson, L. C. & Lozier, M. S. Reconciling the relationship between the AMOC and Labrador Sea in OSNAP observations and climate models. *Geophys. Res. Lett.* **47**, e2020GL089793 (2020).

33. Hirschi, J. & Marotzke, J. Reconstructing the meridional overturning circulation from boundary densities and the zonal wind stress. *J. Phys. Oceanogr.* **37**, 743–763 (2007).

34. McCarthy, G. D. et al. Measuring the Atlantic meridional overturning circulation at 26°N. *Prog. Oceanogr.* **130**, 91–111 (2015).

35. McCarthy, G. D. et al. Sustainable observations of the AMOC: methodology and technology. *Rev. Geophys.* **58**, e2019RG000654 (2020).

36. Yashayaev, I. & Loder, J. W. Further intensification of deep convection in the Labrador Sea in 2016. *Geophys. Res. Lett.* **44**, 1429–1438 (2017).

37. Zou, S., Bower, A., Furey, H., Lozier, M. S. & Xu, X. Redrawing the Iceland-Scotland Overflow Water pathways in the North Atlantic. *Nat. Commun.* **11**, 1–8 (2020).

38. Harden, B. E. et al. Upstream sources of the Denmark Strait Overflow: observations from a high-resolution mooring array. *Deep-Sea Res. Part I* **112**, 94–112 (2016).

39. Hansen, B., Larsen, K. M. H., Hátún, H. & Østerhus, S. A stable Faroe Bank Channel overflow 1995–2015. *Ocean Sci.* **12**, 1205–1220 (2016).

40. Østerhus, S. et al. Arctic Mediterranean exchanges: a consistent volume budget and trends in transports from two decades of observations. *Ocean Sci.* **15**, 379–399 (2019).

41. Aagaard, K., Swift, J. H. & Carmack, E. C. Thermohaline circulation in the Arctic Mediterranean seas. *J. Geophys. Res.: Oceans* **90**, 4833–4846 (1985).

42. Beszczynska-Möller, A., Woodgate, R. A., Lee, C., Melling, H. & Karcher, M. A synthesis of exchanges through the main oceanic gateways to the Arctic Ocean. *Oceanography* **24**, 82–99 (2011).

43. Chafik, L. et al. Discovery of an unrecognized pathway carrying overflow waters toward the Faroe Bank Channel. *Nat. Commun.* **11**, 1–10 (2020).

44. Rossby, T., Flagg, C., Chafik, L., Harden, B. & Søiland, H. A direct estimate of volume, heat, and freshwater exchange across the Greenland-Iceland-Faroe-Scotland Ridge. *J. Geophys. Res.: Oceans* **123**, 7139–7153 (2018).

45. De Steur, L., Hansen, E., Mauritzen, C., Beszczynska-Möller, A. & Fahrbach, E. Impact of recirculation on the East Greenland Current in Fram Strait: results from moored current meter measurements between 1997 and 2009. *Deep-Sea Res. Part I* **92**, 26–40 (2014).

46. Petit, T., Lozier, M. S., Josey, S. A. & Cunningham, S. A. Atlantic deep water formation occurs primarily in the Iceland Basin and Irminger Sea by local buoyancy forcing. *Geophys. Res. Lett.* **47**, e2020GL091028 (2020).

47. Smedsrød, L. H. et al. The role of the Barents Sea in the Arctic climate system. *Rev. Geophys.* **51**, 415–449 (2013).

48. Rhein, M., Steinfeldt, R., Kieke, D., Stendardo, I. & Yashayaev, I. Ventilation variability of Labrador Sea Water and its impact on oxygen and anthropogenic carbon: a review. *Philos. Trans. R. Soc. A: Math., Phys. Eng. Sci.* **375**, 20160321 (2017).

49. Thomas, M. D., Tréguier, A. M., Blanke, B., Deshayes, J. & Volodko, A. A. Lagrangian method to isolate the impacts of mixed layer subduction on the meridional overturning circulation in a numerical model. *J. Clim.* **28**, 7503–7517 (2015).

50. Li, F. et al. Local and downstream relationships between Labrador Sea Water volume and North Atlantic meridional overturning circulation variability. *J. Clim.* **32**, 3883–3898 (2019).

51. Dickson, R. R., Meincke, J., Malmberg, S. A. & Lee, A. J. The “great salinity anomaly” in the northern North Atlantic 1968–1982. *Prog. Oceanogr.* **20**, 103–151 (1988).

52. Belkin, I. M., Levitus, S., Antonov, J. & Malmberg, S. A. “Great salinity anomalies” in the North Atlantic. *Prog. Oceanogr.* **41**, 1–68 (1998).

53. Locarnini R. A. et al. World Ocean Atlas 2013, Volume 1: Temperature. S. Levitus, Ed., A. Mishonov Technical Ed.; NOAA *Atlas NESDIS* 73, 40 pp. (2013).

54. Zweng, M. M. et al. World Ocean Atlas 2013, Volume 2: Salinity. S. Levitus, Ed., A. Mishonov Technical Ed.; NOAA *Atlas NESDIS* 74, 39 pp. (2013).

55. Ridgway, K. R., Dunn, J. R. & Wilkin, J. L. Ocean interpolation by four-dimensional least squares –Application to the waters around Australia. *J. Atmos. Ocean. Tech.* **19**, 1357–1375 (2002).

56. Dunn, J. R. & Ridgway, K. R. Mapping ocean properties in regions of complex topography. *Deep Sea Res Part I Oceanogr. Res.* **49**, 591–604 (2002).

57. Dee, D. P. et al. The ERA-Interim reanalysis: configuration and performance of the data assimilation system. *Q. J. R. Meteorol. Soc.* **137**, 553–597 (2011).

58. Griffies, S. M. et al. OMIP contribution to CMIP6: experimental and diagnostic protocol for the physical component of the Ocean Model Intercomparison Project. *Geosci. Model Dev.* **9**, 3231–3296 (2016).

59. Rio, M. H., Mulet, S. & Picot, N. Beyond GOCE for the ocean circulation estimate: synergistic use of altimetry, gravimetry, and in situ data provides new insight into geostrophic and Ekman currents. *Geophys. Res. Lett.* **41**, 8918–8925 (2014).

60. Lozier, M. S. et al. Meridional overturning circulation and the associated heat and freshwater transports observed by the OSNAP (Overturning in the Subpolar North Atlantic Program) Array from 2014 to 2016. Duke Digital Repository. <https://doi.org/10.7294/r4z60gf0f> (2019).

61. Li, F., Lozier, M. S. & Johns, W. E. Calculating the meridional volume, heat, and freshwater transports from an observing system in the subpolar North Atlantic: observing system simulation experiment. *J. Atmos. Ocean. Tech.* **34**, 1483–1500 (2017).

62. Curry, B., Lee, C. M., Petrie, B., Moritz, R. E. & Kwok, R. Multiyear volume, liquid freshwater, and sea ice transports through Davis Strait, 2004–10. *J. Phys. Oceanogr.* **44**, 1244–1266 (2014).

63. Danabasoglu, G., Large, W. G. & Briegleb, B. P. Climate impacts of parameterized Nordic Sea overflows. *J. Geophys. Res.: Oceans* **115**, 1–29 (2010).

64. Wang, H., Legg, S. A. & Hallberg, R. W. Representations of the Nordic Seas overflows and their large scale climate impact in coupled models. *Ocean Modelling* **86**, 76–92 (2015).

65. Zhang, R. & Thomas, M. Supporting data for “Horizontal circulation across density surfaces contributes substantially to the long-term mean northern Atlantic Meridional Overturning Circulation” [Data set]. Zenodo. <https://doi.org/10.5281/zenodo.4592442> (2021).

66. McCartney, M. S. & Talley, L. D. Warm-to-cold water conversion in the northern North Atlantic Ocean. *J. Phys. Oceanogr.* **14**, 922–935 (1984).

## Acknowledgements

We thank Suki Manabe and Mike Winton for their comments on the manuscript. We thank Raf Dussin for sharing the tool for extracting model grid point positions along high latitude ocean sections. We thank Thomas Rossby and two anonymous reviewers for their suggestions to improve the original submission.

## Author contributions

R.Z. conceived the study, formulated and conducted the numerical experiments, and designed the main analysis approaches. R.Z. and M.T. analyzed the results together. R.Z. wrote the paper with input from M.T.

**Competing interests**

The authors declare no competing interests.

**Additional information**

**Supplementary information** The online version contains supplementary material available at <https://doi.org/10.1038/s43247-021-00182-y>.

**Correspondence** and requests for materials should be addressed to R.Z.

**Peer review information** Primary handling editors: Regina Rodrigues, Heike Langenberg.

**Reprints and permission information** is available at <http://www.nature.com/reprints>

**Publisher's note** Springer Nature remains neutral with regard to jurisdictional claims in published maps and institutional affiliations.



**Open Access** This article is licensed under a Creative Commons Attribution 4.0 International License, which permits use, sharing, adaptation, distribution and reproduction in any medium or format, as long as you give appropriate credit to the original author(s) and the source, provide a link to the Creative Commons license, and indicate if changes were made. The images or other third party material in this article are included in the article's Creative Commons license, unless indicated otherwise in a credit line to the material. If material is not included in the article's Creative Commons license and your intended use is not permitted by statutory regulation or exceeds the permitted use, you will need to obtain permission directly from the copyright holder. To view a copy of this license, visit <http://creativecommons.org/licenses/by/4.0/>.

This is a U.S. Government work and not under copyright protection in the US; foreign copyright protection may apply 2021